JOURNAL OF AIRCRAFT
Vol. 34, No. 5, September–October 1997

Navier–Stokes/Full Potential/Free-Wake Method for Rotor Flows

Mert E. Berkman* and Lakshmi N. Sankar†
Georgia Institute of Technology, Atlanta, Georgia 30332
and
Charles R. Berezin‡ and Michael S. Torok‡
Sikorsky Aircraft Corporation, Stratford, Connecticut 06497

A technique for modeling unsteady three-dimensional compressible viscous flow over lifting rotors in hover and forward flight is described. The flow solver has three modules: 1) a compressible Navier–Stokes solver for modeling the viscous flow over the rotor and the rotor near wake; 2) a compressible potential flow solver for modeling the inviscid, isentropic potential flow regions far away from the rotor, and 3) a Lagrangian model for capturing and convecting the rotor wake once it leaves the Navier–Stokes domain. Results are presented for viscous flow over a two-bladed untwisted rotor and a UH-60A rotor in hover. Good agreement is found with measurements.

Nomenclature

C_Q = rotor torque coefficient
C_T = rotor thrust coefficient
c = blade chord
$\boldsymbol{dl}$ = length of a vortex filament
E, F, G = inviscid fluxes in three directions
M_{tip} = tip Mach number
$\boldsymbol{n}$ = unit normal vector
p = pressure
q = flow property
$\boldsymbol{q}^v$ = induced velocity caused by wake
R = blade radius
R, S, T = viscous fluxes in three directions
$\boldsymbol{r}$ = distance between a vortex filament and the point where induced velocity is calculated
T = temperature
u, v, w = velocity components in x, y, z directions
$\boldsymbol{V}$ = velocity vector
$\boldsymbol{V}_{\text{Grid}}$ = grid velocity
Γ = tip vortex strength
θ_c = collective pitch angle
ξ, η, φ = three directions in the computational domain
ρ = density
σ = solidity
ϕ = velocity potential

Introduction

THE single most determinant factor in rotor performance is the behavior of the shed wake that dominates the rotor acoustics and vibratory loads. At low speeds this skewed helical wake remains close to the helicopter and alters the flowfield around the vehicle. As a result, the biggest challenge in predicting rotorcraft flowfield is the accurate representation of the vorticity in the flowfield in low-speed forward flight. The objective of this study is to develop a general multiblade Navier–Stokes/full potential/free-wake method for the prediction of rotor performance and wake.

The existing finite difference methodologies for rotorcraft aerodynamics can be divided into two categories, depending on their treatment of wake effects. First-generation finite difference codes[1–5] solved the potential, Euler, or Navier–Stokes equations coupled with an external free-or rigid-wake model. In the second-generation Navier–Stokes codes, an attempt was made to capture the shed vorticity and the tip vortex entirely from first principles.[6–8] This approach requires significant computer resources, even when high-order spatial accuracy schemes are used because of the high levels of numerical viscosity present in these schemes, particularly on coarse grids far away from the rotor disk. Although some attempts in the past have been made to reduce computer time through the use of a hybrid Navier–Stokes/full potential method,[9] in such methods the rotor wake is captured by Eulerian approaches and is not adequately resolved away from the rotor. The only exception to these methods is a hybrid Navier–Stokes/full potential method of Moulton and Caradonna,[10] where a Lagrangian approach was used to track the vortex filaments once they leave the Navier–Stokes zone and enter the potential flow zone.

Overview of the Present Work

In this approach, a hybrid method is developed to solve for the flowfield over multiblade rotors in hover or forward flight. In the present study, only the hover calculations are considered. The forward-flight calculations are currently underway.[11]

The flow is divided into three regimes: 1) a small viscous region surrounding individual rotor blades, 2) a potential flow region that carries the acoustic and pressure waves generated by the rotor to far field, and 3) a Lagrangian scheme for capturing the circulation that leaves the viscous region and convecting it away to the far field. Figure 1 shows the Navier–Stokes and potential flow zones, and a typical tip vortex trajectory.

In the viscous region, the unsteady compressible Navier–Stokes equations are solved in a finite volume form. In the inviscid region, the isentropic potential flow equations are solved. The effect of vorticity embedded in the potential flow region is computed using the Biot–Savart law.

Although there are many similarities between the present work and earlier works of Berezin[9] and of Moulton,[10] there are

---

Received Nov. 4, 1996; presented as Paper 97-0401 at the AIAA 35th Aerospace Sciences Meeting, Reno, NV, Jan. 6–9, 1997; revision received Feb. 5, 1997; accepted for publication May 24, 1997.

*Graduate Research Assistant, School of Aerospace Engineering. Student Member AIAA.

†Regents Professor, School of Aerospace Engineering. Senior Member AIAA.

‡Aerodynamics Engineer.

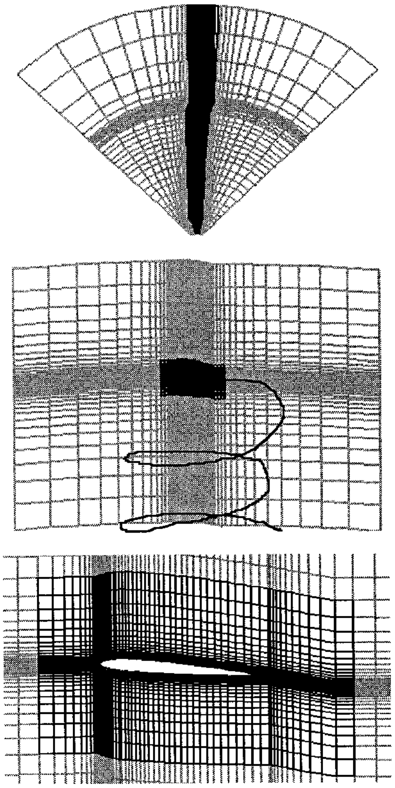

Fig. 1 Grid for four-bladed UH-60A rotor in hover.

several notable differences. For example, in Berezin's work,[9] only the near wake was captured. The effects of far wake had to be implemented as a user-supplied induced angle-of-attack table. In Moulton's work,[10] the formulation allows a potential solver to find both the near-field and induced velocities. However, the Navier–Stokes zone was modeled using a C-grid that extended from one blade periodic boundary to the next, and was large. The present work uses a very small H-grid enclosing the blade that can potentially grow or shrink with time. Finally, the present formulation is cast as an unsteady problem, so that steady and unsteady forward-flight calculations may be done with a single solver. Of course, time-saving approaches such as the use of local time stepping may be used in our work in hover applications to accelerate convergence.

The rest of the paper is organized as follows. The mathematical and numerical formulations are described rather briefly, because these are well developed and have been extensively published.[8,9] A detailed description of how Lagrangian wake is initialized, tracked in time, and updated in strength is also given. The boundaries that separate the two zones must be carefully handled to allow pressure waves to propagate out to the far field without false reflections at the interface. The solver should allow vorticity to enter and leave the zones in a physically consistent manner. These boundary conditions are discussed next. Finally, a number of validations for a two-bladed rotor tested by Caradonna and Tung[12] and for the UH-60A rotor tested by Lorber et al.[13] are presented.

Mathematical and Numerical Formulation

Computational Grid

An H–O grid shown in Fig. 1 is used to model multibladed rotors in hover. For hover cases, only one blade needs to be modeled because the flow is periodic from blade to blade. The rotor element may be a single-element airfoil or a rotor–slat combination. The present analysis is for single-element airfoils.

As previously discussed, the flowfield is divided into two zones, the first zone includes the inviscid potential flow regions away from the individual blades, and the second zone covers a small region around the individual rotor blade. In this second zone, viscous effects are modeled. There is an exact one-to-one matching between the nodes of the two zones at the interfaces. The top view of a grid in a rotor plane, a radial plane, and a close up on viscous zone is shown in Fig. 1. The inner Navier–Stokes zone is distinguished with darker grids. For multibladed rotors in forward flight, there will be several such small zones.

Navier–Stokes Solver

The three-dimensional unsteady, Reynolds-averaged Navier–Stokes equations may be written as

$$\frac{\partial q}{\partial t} + \frac{\partial E}{\partial x} + \frac{\partial F}{\partial y} + \frac{\partial G}{\partial z} = \frac{\partial R}{\partial x} + \frac{\partial S}{\partial y} + \frac{\partial T}{\partial z} \tag{1}$$

In the present work, this equation is solved in the following divergence form:

$$\frac{\partial}{\partial t}\int\!\!\int\!\!\int q \, \mathrm{d}V + \oiint (E\boldsymbol{i} + F\boldsymbol{j} + G\boldsymbol{k})\cdot\boldsymbol{n} \, \mathrm{d}S = \oiint (R\boldsymbol{i} + S\boldsymbol{j} + T\boldsymbol{k})\cdot\boldsymbol{n} \, \mathrm{d}S \tag{2}$$

Equation (2) is valid for arbitrary, but stationary control volume. If the control volume is deforming with respect to time, then additional terms that account for the flux leaving and entering a cell must be added. For example, the mass flux entering a face would be $\oint \rho[\boldsymbol{V} - \boldsymbol{V}_{\mathrm{Grid}}]\cdot\boldsymbol{n} \, \mathrm{d}S$. In such a case, the time derivative should be viewed as the time derivative for a given cell, rather than a conventional partial derivative holding (x, y, z) fixed.

The fluxes crossing the cell face are computed using the Roe solver, with flux properties evaluated at the left and right sides of a given face using a MUSCL scheme.[14] The viscous terms are computed using algebraic averages of flow properties on either side of a cell face. The resulting nonlinear algebraic system of equations for the flow properties are linearized using the information at the previous time level. The resulting linearized system is inverted using an approximate factorization scheme. Details of the solver are found in the dissertation of Bangalore.[8] The Baldwin–Lomax model is used to model turbulence. This solver can be run on a single processor, or distributed over multiple processors over a cluster of workstations. In the present study, the single processor version of the analysis was used.

Potential Flow Solver

The potential flow solver solves the continuity equation

$$\frac{\partial}{\partial t}\int\!\!\int\!\!\int \rho \, \mathrm{d}V + \oiint \rho(\boldsymbol{V} - \boldsymbol{V}_{\mathrm{Grid}})\cdot\boldsymbol{n} \, \mathrm{d}S = 0 \tag{3}$$

where the flow velocity $\boldsymbol{V}$ is made up of three components: freestream velocity, disturbance potential-based velocity, and induced velocity caused by embedded vorticity:

$$\boldsymbol{V} = \boldsymbol{V}_\infty + \nabla\phi + \boldsymbol{q}^v \tag{4}$$

The density is assumed to be related to velocity potential through isentropic gas law, neglecting the temporal variation of $\boldsymbol{q}^v$. The gradient of velocity $\nabla\phi$ may be written as an expression linking the velocity potential at a node (i, j, k) to its 26 neighbors $(i \pm 1, j \pm 1, k \pm 1)$. The resulting system is linear in ϕ, if density is assumed to be known from a previous time step.

A three-dimensional unsteady compressible potential flow solver developed by Sankar et al.[15] is used to solve Eq. (3). It uses a three-factor alternating direction implicit scheme to invert the matrix system for ϕ. The potential flow solver can capture embedded weak shock waves and model the convection of acoustic waves in a time-accurate manner. It cannot, however, capture embedded vortex filaments such as embedded tip vortices. A mechanism must be therefore provided in the flow solver to model this effect.

Wake Model

A rigid or a free-wake model is used to account for the wake effects in full potential zones. The model used in this study only considers the tip vortex, neglecting the inboard vortex sheet and trailed vorticity away from the blade. In future studies, more of the inner wake will be included,[11] and an efficient procedure for the induced velocity proposed by Steinhoff et al.[16] will be used. The helical tip vortices are modeled by a connected series of straight-line elements with azimuthal increments of 10 deg. The classical helical wake (up to 10 revolutions) is used as an initial guess to start the solution process. The strength of the tip vortex is taken to be the bound circulation at a predefined tip radial station (usually 97–99% radii), or the peak bound circulation, and allowed to change from one time level to the next as the loading on the blade changes.

Given the vorticity strength and geometry, the induced velocity can be evaluated. One approach for line elements is the Biot–Savart law:

$$\boldsymbol{q}^{v} = -\sum_{\text{elements}} \frac{\Gamma}{4\pi} \frac{\mathrm{d}\boldsymbol{l} \times \boldsymbol{r}}{|\boldsymbol{r}^{3}|} \tag{5}$$

A Rankine vortex core model[17] with a radius of one-tenth of the blade radius is used. Using Eq. (5), the induced velocities at all full potential nodes are computed. The induced velocity then is included in the potential flow analysis [Eq. (3)]. Navier–Stokes nodes will receive the effect of this velocity field through interface conditions.

The free-wake model is developed simply by relaxing the first revolution of wake elements so that they move with the local flow velocity. The remaining wake elements are nonmoving wake elements and placed appropriately based on the position of the last free-wake marker. The main advantage of the rigid-wake model is that the induced velocity coefficients (by Biot–Savart law) need to be calculated only once because the wake structure remains unchanged. In free-wake models, because the filaments move at each iteration, these coefficients have to be updated. This calculation consumes more than 45 times the CPU required for a single time step. Thus, it becomes prohibitively expensive to update wake information at every time step. Besides, numerous researchers had encountered free-wake instability, when they updated the wake structure continually. Therefore, in this study, at every time step, only the location of the filaments are tracked and the wake-induced velocities are recomputed at all nodes after every 5–15 deg of blade rotation.

Boundary Conditions

In this formulation, there are four types of boundary conditions that must be addressed: 1) solid surface boundary conditions at the rotor surface, 2) far-field boundary conditions, 3) boundary conditions for acoustic waves that cross the Navier–Stokes/full potential interface, and 4) boundary conditions for vorticity that leaves and/or re-enters a zone.

Solid Surface Boundary Conditions

The no-slip conditions are enforced. For a rotor this simply means that the velocity of the fluid is equal to the velocity of the solid. The surface pressure and temperature gradients $\partial p/\partial n$ and $\partial T/\partial n$ were set to zero at the solid surface.

Far-Field Boundary Conditions

In the present approach, the far field is usually located one or more rotor diameters away from the rotor disk, and contamination of the solution because of the reflection of acoustic waves at the far field is not a major consideration. The code in its present form sets the disturbance potential ϕ to be zero at these boundaries. This assumption that all disturbances vanish at the far-field boundaries, however, violates the global momentum and energy balance. More accurate boundary conditions, e.g., those based on mass sink, are being considered. For forward-flight applications, flow quantities at the block boundaries (lying in azimuthal planes) are transferred from block-to-block. All blocks are analyzed because the flow is not periodic.

Boundary Conditions for Modeling Acoustic Waves that Cross the Navier–Stokes/Full Potential Interface

The following coupling of Navier–Stokes and full potential zones was originally developed by Sankar et al.[18] and shown to pass information through interface boundaries accurately for fixed and rotary wing solvers using C–H grids.[9,18]

The Navier–Stokes and the full potential zone are required to overlap each other at least by one node in the present approach. Consider a point P with index $(i,\ j\ ,\ k)$ shown in Fig. 2. The box around node P represents cell faces. The point immediately underneath $(i,\ j,\ k - 1)$ lies in the Navier–Stokes zone, while the point immediately above it $(i,\ j,\ k + 1)$ lies in the potential flow zone. The point $(i,\ j,\ k)$ itself is solved for twice, once using the Navier–Stokes solver, and again using the full potential flow solver.

At the interface $(i,\ j,\ k - 1/2)$ the potential flow solver requires ρ and V_n so that the flux crossing boundary $\rho V_n \Delta S$ can be computed. In this work, these quantities were computed by averaging the Navier–Stokes values at the node $(i,\ j,\ k)$ and the node $(i,\ j,\ k - 1)$ immediately underneath it. Thus, the Navier–Stokes code supplies a Neumann type of boundary condition to the potential flow solver for $\partial\phi/\partial n$. The Navier–Stokes code does not transfer information about the tangential components of velocity, i.e., vorticity, directly to the potential flow solver.

When applying the Navier–Stokes solver to P, all of the flow properties are needed $(\rho,\ u,\ v,\ w,\ p)$ at $(i,\ j,\ k + 1)$, and at $(i,\ j,\ k + 2)$. These were obtained by computing $\nabla\phi$ using Eq. (6), and then applying Eq. (7) to get T, and finally applying the isentropic law to get ρ and p, using Eq. (8):

$$\begin{aligned} u &= \phi_\xi \xi_x + \phi_\eta \eta_x + \phi_\varphi \varphi_x \\ v &= \phi_\xi \xi_y + \phi_\eta \eta_y + \phi_\varphi \varphi_y \\ w &= \phi_\xi \xi_z + \phi_\eta \eta_z + \phi_\varphi \varphi_z \end{aligned} \tag{6}$$

$$C_P T + \frac{u^2 + v^2 + w^2}{2} + \phi_t = C_P T_\infty + \frac{V_\infty^2}{2} \tag{7}$$

$$\frac{T}{T_\infty} = \left(\frac{\rho}{\rho_\infty}\right)^{\gamma - 1} \tag{8}$$

where ξ_x, η_x, φ_x are metrics that transform the body-fitted grid to the computational grid.

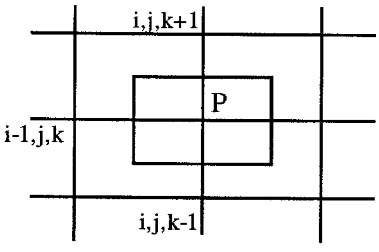

Fig. 2 Computational nodes and cells.

Similar expressions are developed in this study for the interface boundaries that lie in azimuthal planes extending the methodology to H-O and H-H topologies.

Boundary Conditions for Vorticity Leaving the Navier–Stokes Zone and Entering the Potential Flow Zone

The potential flow zone receives vorticity in the form of a distributed vortical flowfield. The initial portions of the tip vortex following its generation at the blade are solved inside the Navier–Stokes zone. At the interface, it is converted into a concentrated tip vortex made up of wake markers that are tracked using a Lagrangian scheme. Of course, some numerical diffusion of the vortex is inevitable in the inner zone. Knowledge of Γ and the marker positions mentioned earlier is enough to compute the induced velocity associated with these markers.

Boundary Conditions for Vorticity Leaving the Potential Zone and Entering the Navier–Stokes Zone

Occasionally, a vortex filament of strength Γ will enter the Navier–Stokes zone. No special treatment is required in this condition because the effect of the tip vortex entering (or passing close to) the Navier–Stokes zone is felt through the Navier–Stokes/full potential interface boundary conditions.

Results and Discussion

The preceding algorithm has been coded and tested for a rectangular hovering rotor, and for a modern, highly twisted rotor with a swept tip. Thus, these two applications bracket a variety of hover applications and rotors of interest to the industry.

Caradonna–Tung Rotor in Hover

The hybrid hover solver has been tested for several nonlifting and lifting hover cases, experimentally studied by Caradonna and Tung.[12] They considered a two-bladed untwisted, rotor of rectangular planform. The blades have NACA 0012 sections and an aspect ratio of 6. Surface pressure data are available at a number of chordwise locations at several radial locations for code validation.

An H–H grid with 133 azimuthal, 43 radial, and 62 normal nodes is used as computational domain. The domain covers half of the rotor disk, and extends one blade radius R, above and below the rotor plane, and over one-half radius in the spanwise direction from the blade tip. Approximately 29% of the nodes fall into the Navier–Stokes zone. The Navier–Stokes zone covers approximately one-half chord upstream and one-half chord downstream of the blade. It extends to the far boundary in a spanwise direction. It is possible to place another interface boundary in the radial direction and further reduce the number of Navier–Stokes nodes. However, it is found that the small CPU savings does not justify adding the extra interface boundary and further complications to the process.

The code is first validated for a nonlifting case where no wake modeling is needed. Figure 3 compares measured surface

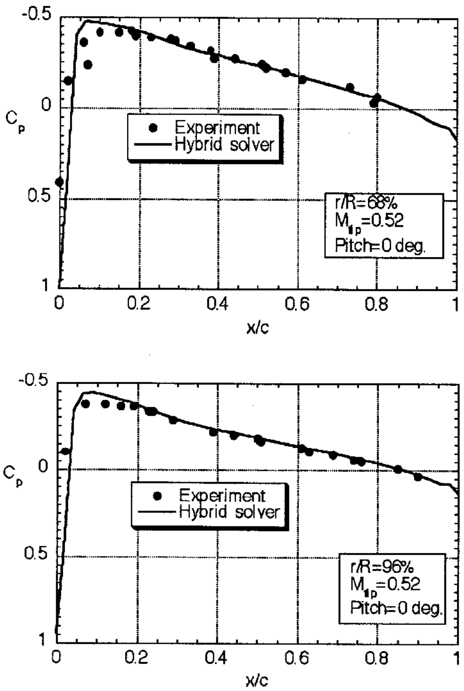

Fig. 3 Surface pressures for nonlifting case.

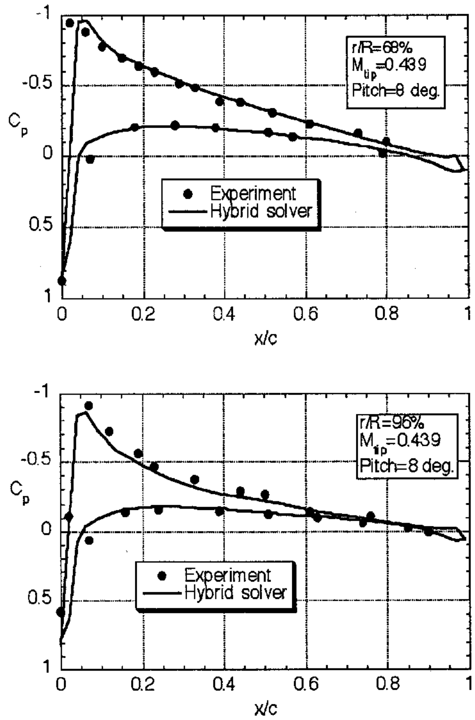

Fig. 4 Surface pressure coefficients.

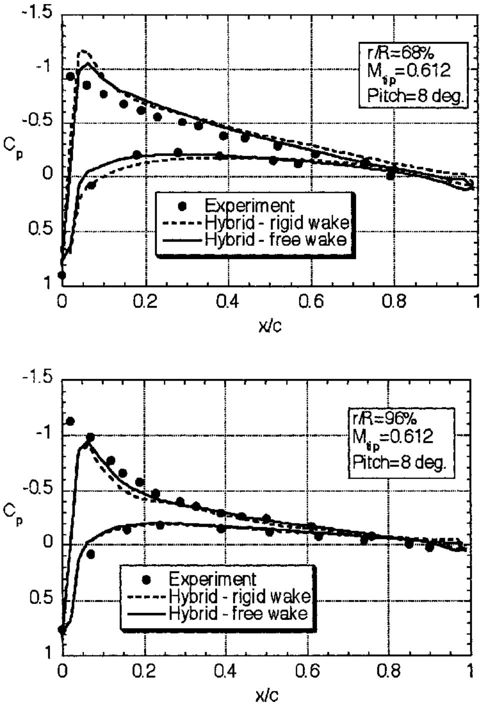

Fig. 5 Surface pressure coefficients.

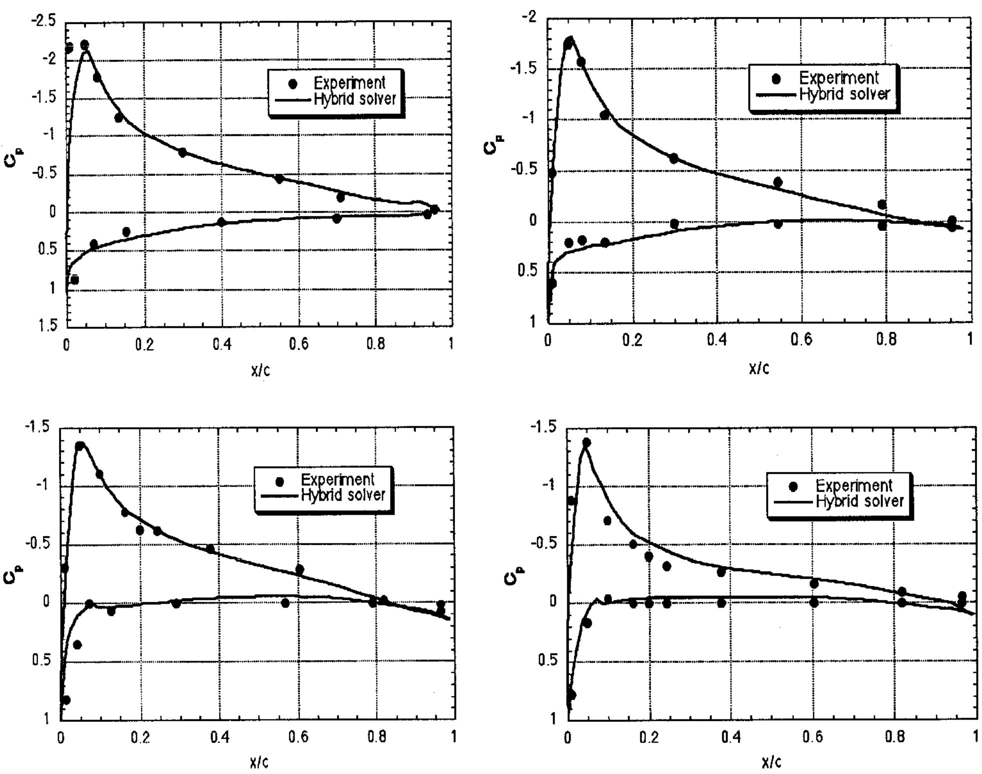

Fig. 6 Surface pressure coefficients for UH-60A rotor at various radial stations.

pressures on the blade to computed values at two radial locations. The test was conducted at a tip Mach number of 0.52. Good agreement on pressure indicates successful coupling of the two zones.

Figure 4 shows the surface pressure distributions at two different spanwise stations, 68 and 96% blade radius. The rotor has a collective pitch of 8 deg with a tip Mach number of 0.439. Here, the free-wake model is employed with the recomputation of wake geometry and the associated induced velocities 11 times. The tip vortex strength at every time step is set to the current bound circulation at 97% blade radius at the start. After several iterations, the peak bound circulation may be used.

A higher tip speed is considered next. Figure 5 shows experimental data and numerical results. The experimental thrust coefficient is 0.00455, and the computed values are 0.00393 with free wake and 0.00496 with rigid-wake options. Here, no trimming was performed to match thrust coefficient values. Trimming the solution (by changing collective pitch) and refining grid in the tip region may improve the accuracy.

In general, good agreement is observed between the measurements and the calculations for the Caradonna–Tung rotor. It is seen that the free-wake model improves the quality of the solution. It corrects the rigid vortex behavior of the overprediction of loads midboard and the underprediction near the tip sections. The free-wake model captures the tip vortex position fairly well compared to experimental measurements. The tip vortex is measured to contract 10% radii and to descend 0.3*R* after a full blade revolution. The corresponding numerical values are 7% and 0.34*R*. The CPU time increase with the free-wake option was roughly 10% over the rigid-wake option.

UH-60A Rotor in Hover

The hover solver is also validated for a typical current generation rotor, the four-bladed UH-60A rotor. The blade has an aspect ratio of 15.3 and a maximum twist of 13 deg. It has a rearward sweep of 20 deg starting from a rotor radius of 93%. The blade is made up of two airfoil sections, SC1095 as the main airfoil and SC1095R8 section in the midspan.[13] The H–O grid is shown in Fig. 1 and has 90 points in azimuthal, 43 in spanwise, and 80 in normal directions. Approximately 37% of the nodes lie in the Navier–Stokes zone, and typically seven points lie inside the boundary layer.

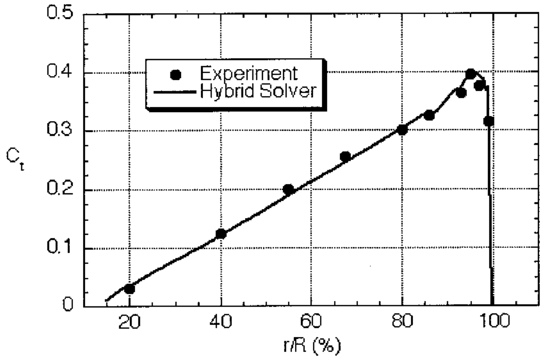

Fig. 7 Radial distribution of section normal force coefficient for UH-60A blade.

In these calculations, the tip vortex strength was chosen initially to be the bound circulation at 99% radius. After several hundred iterations, the peak bound circulation was used as the tip vortex strength. The calculations were started with a rigid, noncontracting wake of 10 revolutions. At every 10 deg of blade rotation, the wake geometry and the wake-induced velocity updates were done during the time marching process, as discussed previously.

Figure 6 shows the surface pressures at four radial stations. The rotor is at a collective pitch angle of 10 deg and a tip Mach number of 0.628. The loads are in very good agreement with the experimental measurements. No trimming was done in these computations.

Figure 7 shows the spanwise thrust distribution over the blade. The numerical values are in good agreement with experimental measurements. The numerical value of C_T/σ = 0.0084 compares well with experimental 0.0085. However, the power consumed by the rotor is overestimated by the solver.

The torque, C_Q/σ is found as 0.00076 as opposed to 0.00070 from experiments.

A typical hover solution requires about 15 h of CPU time on an HP 735 Workstation. The convergence is reached when the residuals drop by three orders of magnitude. Approximately a 50% CPU reduction is achieved for the test cases using the hybrid methodology (with rigid- or free-wake option) compared to the stand-alone Navier–Stokes solver,[8] without degrading the quality of the solution. Free-wake option increases the CPU time by 10% compared to the rigid wake option.

Concluding Remarks

A hybrid Navier-Stokes/full potential solver with a Lagrangian treatment of the far wake has been developed, and preliminary validation studies have been done. This formulation is written in a fully unsteady form, permitting a straight-forward extension to forward-flight analysis. The Navier–Stokes region can be kept very small, leading to lower CPU times.

Additional code validations for rotors in hover are needed. These should be followed by forward-flight studies. Recent advancements in the methodology such as a fifth-order-accurate spatial differencing scheme and the distribution of calculations over multiple processors should be done. With these enhancements, this solver should prove to be a useful and efficient tool to the rotorcraft industry.

Acknowledgments

The first two authors were supported by a contract from the Sikorsky Aircraft Corporation.

References

[1] Caradonna, F. X., and Tung, C., "Experimental and Analytical Studies of a Model Helicopter Rotor in Hover," *Vertica*, Vol. 5, 1981, pp. 149–161.

[2] Sankar, L. N., and Prichard, D., "Solution of Transonic Flow Past Rotor Blades Using the Conservative Full Potential Equation," AIAA Paper 85-5012, Oct. 1985.

[3] Sankar, L. N., Wake, B. E., and Lekoudis, S. G., "Solution of the Unsteady Euler Equations for Fixed and Rotor Wing Configurations," *Journal of Aircraft*, Vol. 23, No. 4, 1986, pp. 283–289.

[4] Agarwal, R. K., and Desse, J. E., "Euler Calculations for Flowfield of a Helicopter Rotor in Hover," *Journal of Aircraft*, Vol. 24, No. 4, April 1987, pp. 231–238.

[5] Wake, B. E., and Sankar, L. N., "Solution of Navier-Stokes Equations for the Flow over a Rotor Blade," *Journal of the American Helicopter Society*, Vol. 34, No. 2, 1989, pp. 13–22.

[6] Srinivasan, G. R., and McCroskey, W. J., "Navier-Stokes Calculations of Hovering Rotor Flowfields," *Journal of Aircraft*, Vol. 25, No. 10, 1988, pp. 865–874.

[7] Strawn, R. J., and Barth, J. T. "A Finite-Volume Euler Solver for Computing Rotary-Wing Aerodynamics on Unstructured Meshes," *Proceedings of the 48th Annual Forum of the American Helicopter Society* (Washington, DC) American Helicopter Society, Alexandria, VA, 1992.

[8] Bangalore, A., and Sankar, L. N., "Forward Flight Analysis of Slatted Rotors Using Navier-Stokes Methods," AIAA Paper 96-0675, Jan. 1996.

[9] Berezin, C. R., and Sankar, L. N., "An Improved Navier-Stokes/Full Potential Coupled Analysis for Rotors," *Mathematical Computational Modeling*, Vol. 19, Nos. 3/4, 1994, pp. 125–133.

[10] Moulton, M. A., Hafez, M. M., and Caradonna, F. X., "Zonal Procedure for Predicting the Hovering Performance of a Helicopter," *ASME Journal*, Vol. 184, June 1994, pp. 151–161.

[11] Berkman, M. E., "An Integrated Navier-Stokes-Full Potential-Free Wake Method for Rotor Flows," Ph.D. Dissertation, Georgia Inst. of Technology, Atlanta, GA, 1997.

[12] Caradonna, F. X., and Tung, C., "Experimental and Analytical Studies of a Model Helicopter Rotor in Hover," NASA TM-81232, Sept. 1981.

[13] Lorber, P. F., Stauter, R. C., and Landgrebe, A. J., "A Comprehensive Hover Test of the Airloads and Airflow of an Extensively Instrumented Model Helicopter Rotor," *Proceedings of the 45th Annual Forum of the American Helicopter Society*, American Helicopter Society, Alexandria, VA, 1989.

[14] Van Leer, B., "Towards the Ultimate Conservative Difference Scheme, a Second Order Sequel to Godunov's Method," *Journal of Computational Physics*, Vol. 32, 1979.

[15] Sankar, L. N., Malone, J. B., and Tassa, Y., "An Implicit, Conservative Algorithm for Steady and Unsteady Transonic Potential Flows," *Proceedings of the AIAA 5th Computational Fluid Dynamics Conference*, AIAA, New York, 1981, pp. 199–212.

[16] Steinhoff, J., and Ramachandran, K., "Free-Wake Analysis of Compressible Rotor Flows," *AIAA Journal*, Vol. 28, No. 2, 1989, pp. 426–431.

[17] *2GCHAS Theory Manual*, Vol. 2, U.S. Dept. of the Army, Aeroflightdynamics Directorate, Ames Research Center, Moffett Field, CA, July 1992, Chap. 5.

[18] Sankar, L. N., Bharadvaj, B. K., and Tsung, F.-L., "Three-Dimensional Navier-Stokes/Full Potential Coupled Analysis for Transonic Viscous Flow," *AIAA Journal*, Vol. 31, No. 10, 1993, pp. 1857–1862.